RADIO SCIENCE, VOL. 44, XXXXXX, doi:10.1029/2008RS003863, 2009

Array rotation aperture synthesis for short-range imaging at millimeter wavelengths

B. M. Lucotte,[1] B. Grafulla-González,[2] and A. R. Harvey[1]

Received 31 March 2008; revised 1 August 2008; accepted 28 October 2008; published XX Month 2009.

[1] Millimeter-wave interferometric synthetic aperture imagers are currently being developed for short-range applications such as concealed weapons detection. In contrast to the traditional snapshot imaging approach, we investigate the potential of mechanical scanning between the scene and the array in order to reduce the number of antennas and correlators. We assess the trade-off between this hardware reduction, the radiometric sensitivity and the imaging frame rate of the system. We show that rotational scanning achieves a more uniform coverage of the (u, v) plane than the more conventional linear scanning. We use a genetic algorithm to optimize two-dimensional arrays for maximum uniform (u, v) coverage after a rotational mechanical scan and demonstrates improvements in the array point spread function. Imaging performance is assessed with simulated millimeter-wave scenes. Results show an increased image quality is achieved with the optimized array compared with a conventional power law Y-shaped array. Finally we discuss the increased demands on system stability and calibration that the increased acquisition time of the proposed technique places.

Citation: Lucotte, B. M., B. Grafulla-González, and A. R. Harvey (2009), Array rotation aperture synthesis for short-range imaging at millimeter wavelengths, *Radio Sci.*, *44*, XXXXXX, doi:10.1029/2008RS003863.

1. Introduction

[2] Passive and semipassive mm-wave imaging techniques are currently receiving considerable attention for short-range imaging, such as personnel scanners, due to their ability to detect concealed weapons through obscurants such as clothing [*Sheen et al.*, 2001; *Appleby*, 2004; *Harvey and Appleby*, 2003]. In contrast to conventional real-aperture imaging systems, synthetic aperture imaging enables images with an infinite depth of field to be recorded using an array that is sparse and essentially planar. For spaceborne remote sensing applications, synthetic aperture imagers have traditionally been considered for the recording of high-spatial-resolution images in a single snapshot. Snapshot operation necessarily requires a large number of antennas. This not only results in a high cost but also contributes to calibration difficulties because of mutual coupling at short baselines. By reducing the number of antennas, one therefore decreases the amount of mutual coupling between receivers. In practice this should simplify the calibration process. It is highly desirable therefore to reduce the antenna count without adversely affecting the spatial resolution of the imager. To that end it is possible to take advantage of a relative motion between the array and the source. In Earth rotation synthesis [*Thompson et al.*, 2001], a technique used in radio-astronomy, the motion is naturally provided by the rotation of the earth relative to the source. For near-field techniques, Synthetic Aperture Radar (SAR) and RADiometric Synthetic Aperture Radar (RADSAR) [*Edelsohn et al.*, 1998], the motion is provided by an airborne or spaceborne platform in translation relative to the source. Since the visibility samples are recorded in time-sequence, the reduction in antenna-count is achieved at the cost of either a reduced imaging frame-rate or a reduced radiometric sensitivity.

[3] In this paper we propose a technique that we call 'array rotation aperture synthesis' that provides the low antenna-count of Earth-rotation synthesis whilst enabling the near-field operation required in short-range applications such as personnel scanning.

[4] In section 2 we remind the fundamental imaging equations and image reconstruction algorithms for near-

[1]School of Engineering and Physical Sciences, Heriot-Watt University, Edinburgh, UK.

[2]Research Department, New Technology Multimedia, Ericsson AB, Lund, Sweden.

0048-6604/09/2008RS003863$11.00

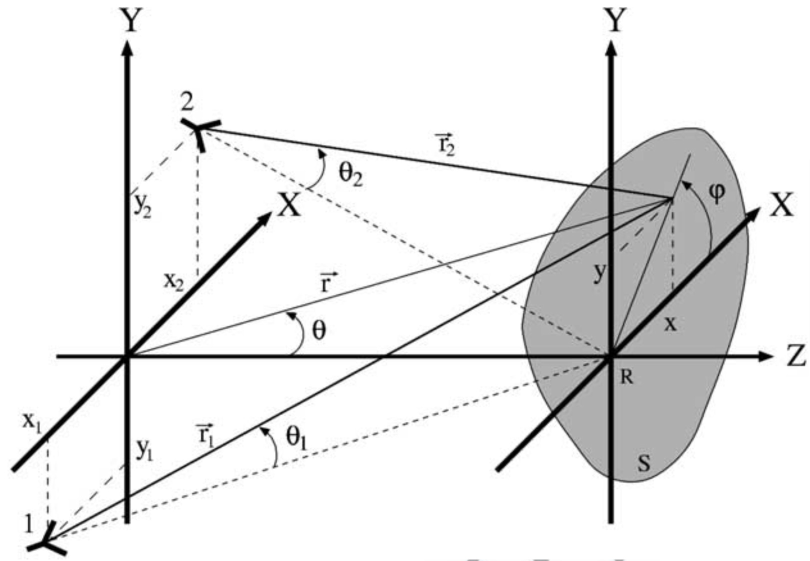

Figure 1. Antenna configuration. The source S is in the far-field of the antennas but in the near-field of the baseline formed by antennas 1 and 2.

field imaging [*Peichl et al.*, 1998], before considering the fundamental requirements of the array for adequate sampling of the near-field image spatial frequencies. We then describe the trade-off between radiometric sensitivity, imaging frame rate and antenna-count. In comparison to a snapshot aperture synthesis radiometer, the time-sequential recording of n_t visibility data sets enables the number of antennas to be reduced by a factor of approximately $\sqrt{n_t}$ without reduction in spatial resolution or sampling density. Section 3 presents a discussion of the considerations involved in the system design and the advantages of rotational scanning over linear scanning are shown. Antenna arrays are optimized by use of a genetic algorithm (GA) [*Haupt*, 1995; *Marcano and Duràn*, 2000] for maximally uniform (u, v) coverage after rotational scanning. The imaging performances of the array are assessed using simulated millimeter-wave scenes and are compared with those achieved with a conventional power law Y-shaped array. Section 4 presents a discussion on the increased demands on system stability and calibration due to increased acquisition time. Conclusions are presented in section 5.

2. Imaging Relations

2.1. Visibility Function

[5] In aperture synthesis one aims to record the image of the brightness temperature distribution of a radiating source with an array of antennas. This image is formed by measuring the correlations between multiple pairs of antenna signals. This measurement is called the visibility function. Conventional synthetic aperture imagers record $N(N-1)$ samples of the complex visibility function in a snapshot using N antennas. Figure 1 shows a simple antenna configuration with $N = 2$, recording a source with a brightness temperature distribution $T_B(\vec{r})$, where $\vec{r}$ is the vector from the origin of the antenna array to a point on the source.

[6] We aim to reduce the number of antennas so as to reduce the system cost and to ease the calibration problem. We will show that this can be achieved by mechanically scanning the array relative to the source and recording the visibility samples in a time sequence. We recall that in the far-field the spatial frequency recorded by a pair of antennas is equal to the length of this baseline measured in wavelengths and projected onto a plane normal to the direction of the source. Since this projection varies with the direction of the source, it is possible to record several spatial frequencies with a single baseline in a time-sequence. The modus-operandus of the Earth-rotation-synthesis technique [*Thompson et al.*, 2001], used in radio astronomy, follows from this principle. The visibility function for a pair of antennas denoted by indices n and m is described by *Peichl et al.* [1998]:

$$\mathcal{V}_{nm} = \frac{k_B \Delta\nu}{\sqrt{\Omega_n \Omega_m}} \int \int_S T_B(\vec{r}) K_{nm}(\vec{r}) \cdot F_W(\Delta r_{nm}, \Delta\nu) e^{-\frac{j2\pi}{\lambda_0}\Delta r_{nm}} dS. \quad (1)$$

where:

$$K_{nm}(\vec{r}) = \frac{1}{\| \vec{r}_n \| \| \vec{r}_m \|} \sqrt{P_n(\vec{r}) P_m(\vec{r}) \cos\theta_n \cos\theta_m}, \quad (2)$$

$$\Delta r_{nm} = \| \vec{r}_n \| - \| \vec{r}_m \|, \quad (3)$$

$$\| \vec{r}_n \| = \sqrt{(x_n - x)^2 + (y_n - y)^2 + R^2}, \quad (4)$$

$$= r\sqrt{1 - 2\left(\frac{x_n}{r}\sin\theta\cos\varphi + \frac{y_n}{r}\sin\theta\sin\varphi\right) + \left(\frac{x_n}{r}\right)^2 + \left(\frac{y_n}{r}\right)^2}. \quad (5)$$

k_B is the Boltzmann constant, $\Delta\nu$ is the bandwidth of the antenna channels, Ω_n and Ω_m are the beam solid-angles of antenna n and m, respectively, $T_B(\vec{r})$ is the brightness temperature distribution of the source, $K_{nm}(\vec{r})$ is an amplitude term due to the power patterns of antenna n and m, $P_n(\vec{r})$ and $P_m(\vec{r})$ denote the antenna power pattern of antenna n and m, respectively. The antennas can be focused on specific point source, as shown in Figure 1. The angles between a point source at location $\vec{r}$ and the beam center of antennas n and m is denoted by θ_n and θ_m, respectively. It is assumed that the scene is in the far-field of the array elements, but in the near-field of the array. F_W is the fringe-wash function and depends on the frequency response of the antenna channels and the path difference Δr_{nm} between the point source at $\vec{r}$ and antennas n and m. Note the dependance of Δr_{nm} on $\vec{r}$ has been omitted to simplify the notations. The expression for the fringe wash function for antenna channels with constant gain over the bandwidth $\Delta\nu$ is:

$$F_W(\Delta r_{nm}, \Delta\nu) = \frac{\sin \pi\Delta\nu\Delta r_{nm}/c}{\pi\Delta\nu\Delta r_{nm}/c}. \quad (6)$$

For wide-band signals, of the order of 10 GHz at a center frequency ν_0 = 94 GHz for example, the first nulls of the fringe wash function can be located within the field-of-view (FoV), e.g., ≈30°. This results in a degradation in the signal-to-noise ratio (SNR) of the visibility samples measured, and also of the reconstructed image. One possible solution to reduce this degradation is to introduce artificial delay lines into one antenna channel of each baseline so as to translate the fringe-wash function in azimuth. Maximum signal power can then be recorded over the entire FoV by appropriately choosing these time delays. For a single baseline, the lost signal is recovered by summing all these translated, fringe-washed interference patterns. Another approach consists in splitting the wide bandwidth signal into a set of narrow band signals that have a fringe wash term approximately constant over the imaging FoV. The narrow band signals must be correlated separately and an image is formed at each subband. These subband images have higher noise levels than the full bandwidth image but can be averaged together to reduce the noise back to the same level.

[7] Equation (1) represents a projection of the brightness distribution onto a set of weighted interference patterns. When the source is in the far-field of the array, these interference patterns are complex exponentials and are invariant in the direction orthogonal to the baseline. However, when the source is in the near-field of the array, the frequencies of these interference patterns are chirped and the orientation of the fringes is spatially variant over the source extent.

2.2. Image Reconstruction Algorithm

[8] When the scene is in the near-field of the array, the image can be reconstructed by performing the cross-correlation between the visibility function and a function $\Phi_{nm}(\vec{r})$ [*Peichl et al.*, 1998]:

$$\widehat{T}_B(\vec{r}) = \frac{1}{N(N-1)} \sum_{\substack{n=1 \\ n \neq m}}^{N} \sum_{m=1}^{N} \mathcal{V}_{nm} \Phi^*_{nm}(\vec{r}). \quad (7)$$

where:

$$\Phi_{nm}(\vec{r}) = \frac{e^{-\frac{j2\pi}{\lambda_0}\Delta r_{nm}}}{K_{nm}(\vec{r})}. \quad (8)$$

We denote the point-spread-function (PSF) at $\overrightarrow{r_0}$ by $PSF_0(\vec{r})$ and by Δr_{0nm} the path difference at that point for the baseline (n, m). Using equations (7) and (8) we obtain:

$$PSF_0(\vec{r}) = \frac{1}{N(N-1)} \sum_{\substack{n=1 \\ n \neq m}}^{N} \sum_{m=1}^{N} \frac{K_{nm}(\vec{r}_0)}{K_{nm}(\vec{r})} e^{\frac{j2\pi}{\lambda_0}(\Delta r_{0nm} - \Delta r_{nm})}.$$

For small antennas, of the order of a wavelength, and for short-range personnel scanning applications one can approximate the term $K_{nm}(\overrightarrow{r_0})/K_{nm}(\vec{r})$ to unity over the FoV; typically 30°. Hence equation (8) becomes:

$$PSF_0(\vec{r}) = \frac{1}{N(N-1)} \sum_{\substack{n=1 \\ n \neq m}}^{N} \sum_{m=1}^{N} e^{\frac{j2\pi}{\lambda_0}(\Delta r_{0nm} - \Delta r_{nm})},$$

$$= \frac{2}{N(N-1)} \sum_{n=1}^{N} \sum_{m=n+1}^{N} \cos\left[\frac{2\pi}{\lambda_0}(\Delta r_{0nm} - \Delta r_{nm})\right]. \quad (9)$$

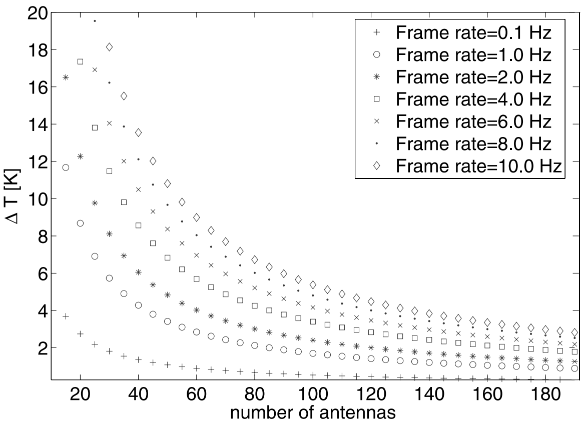

Figure 2. Radiometric sensitivity achieved by a synthetic aperture radiometer including various amounts of scanning. $T_O = 300$ K, $T_R = 500$ K, $\Delta v = 15$ GHz, $M = N(N-1)n_t \approx 36{,}500$.

2.3. Spatial Resolution and Sampling Requirements

[9] We denote by u and v the spatial frequencies recorded by the interferometer, and D the longest baseline of the array. When imaging in the near-field, i.e., when the condition $D^2/\lambda_0 \ll R$ does not hold, the stationary phase principle can be used to provide a first-order approximation of the spatial frequencies (u, v) recorded at a position $\vec{r}$:

$$u(\vec{r}) = \frac{1}{\lambda_0}\frac{\partial \Delta r_{nm}}{\partial \theta}\bigg|_{\varphi=0}, \quad v(\vec{r}) = \frac{1}{\lambda_0}\frac{\partial \Delta r_{nm}}{\partial \theta}\bigg|_{\varphi=\pi/2}. \tag{10}$$

To simplify the analysis we consider the longest baseline of the array as horizontal. Using equation 10 the cutoff spatial frequency $u_{\max}$ of this array is given by:

$$u_{\max} = \frac{D}{\lambda_0}\frac{1}{\sqrt{1+\frac{D^2}{4R^2}}}. \tag{11}$$

To restrict the aliased responses to regions outside the synthesized map, the sampling period Δu and Δv of the Fourier domain must obey the Nyquist sampling requirements:

$$\Delta u \leq \frac{1}{2\sin\theta_{\max}}, \quad \Delta v \leq \frac{1}{2\sin\theta_{\max}}. \tag{12}$$

where $\theta_{\max}$ is the maximum zenith angle within the FoV. In the case of a one-dimensional imager, the minimum number of samples M required in the Fourier interval [0, $u_{\max}$] is:

$$M = \frac{u_{\max}}{\Delta u} = \frac{D}{\lambda_0}\frac{2\sin\theta_{\max}}{\sqrt{1+\frac{D^2}{4R^2}}}. \tag{13}$$

For a representative system used in personnel scanning, a diffraction-limited system with an aperture diameter of 0.7 m is used as a reference. For a source at close range, e.g., 2 m, and a center frequency ν_0 = 94 GHz, the radius of the Airy disk is approximately 11 mm. As an example We consider a 28° FoV, ie $\theta_{\max}$ = 14°. In this case, the number of measurements M required to Nyquist sample the (u, v) plane with a cutoff frequency $u_{\max}$ is approximately 36,500. A conventional interferometric array would require 192 elements to record the visibility samples in a snapshot. We aim to reduce this antenna-count by a factor of 10 to reduce the system complexity, cost and calibration process.

2.4. Radiometric Sensitivity and Trade-Offs

[10] The radiometric sensitivity achieved with a synthetic aperture imager depends on the source distribution and the redundancies in the spatial frequencies measured by the array. For a uniform source and a zero-redundancy array, the radiometric sensitivity at the bore-sight pixel of the image is given by *Ruf et al.* [1988]:

$$\Delta T = (T_O + T_R)\left(\frac{M}{2\Delta\nu\tau}\right)^{1/2}. \tag{14}$$

where $M = N.(N-1)$, N is the number of antennas, T_O and T_R are the received brightness temperature and the noise temperature of the receivers, respectively, τ is the integration time of the receivers. A mechanical scan of the array performs a time-sequential multiplexing of the baselines and therefore enables a reduction in antenna-count. An N-elements antenna-array, scanning a source at n_t successive positions, records $N(N-1)n_t$ visibility samples in the time $n_t\tau$. This represents a reduction in antenna-count by a factor of $\sqrt{n_t}$. Assuming continuous integration, the integration time τ is related to the frame rate F of the imager as follows:

$$\tau = \frac{1}{n_t F} = \frac{N(N-1)}{M.F}. \tag{15}$$

Combining equations (14) and (15) the radiometric sensitivity is expressed as a function of N and F:

$$\Delta T = (T_O + T_R)\left(\frac{F}{2\Delta\nu N(N-1)}\right)^{1/2} M. \tag{16}$$

Equation (16) shows that reducing the number of antennas by a factor of $\sqrt{n_t}$ degrades the radiometric

Table 1. Trade-Offs Between the Antenna-Count Reduction, the Radiometric Sensitivity ΔT, and the Frame Rate F of the Imager

F (Hz)	0.1		1		2		4		6		8		10	
ΔT (K)	N	n_t	N	n_t	N	n_t	N	n_t	N	n_t	N	n_t	N	n_t
0.9	61	10	192	1										
1	54	13												
2	27	52	86	5										
4	14	201	43	20	61	10	86	5					136	2
6			29	45	40	23	56	12	68	8	79	6	86	5
8	7	872	22	79	30	42	43	20	52	14	61	10	68	8
10	6	1221	17	135	24	66	34	33	42	21	48	16	54	13

sensitivity by the same factor, or alternatively degrades the imaging frame-rate by a factor of n_t. Therefore there is a trade-off between the reduction in antenna-count, the radiometric sensitivity and the frame rate of the imager. Figure 2 and Table 1 show the radiometric sensitivity achieved with various degrees of scanning between the source and the array. These results are obtained using T_O = 300 K, T_R = 500 K, $\Delta\nu$ = 15 GHz, $M = N(N-1)n_t \approx 36{,}500$ and show, e.g., that an image with ΔT = 0.9 K can be recorded at a frame rate of 1 Hz with a 192 antenna-array. Alternatively an image with the same ΔT can be recorded in a time-sequence with a 61 antenna-array at a frame-rate of 0.1 Hz.

3. System Design

[11] In the previous section we have discussed the various trade-offs between the radiometric sensitivity, the frame rate of the imager and the antenna-count. We now consider the system design, and the array motion and optimization in particular. Optimizing arrays with large antenna numbers N is a complex task because the dimension of the search space is $2N$ for an array operating in a snapshot and $2Nn_t$ when a scan is included. Although the optimal system ideally requires optimizing the array and its motion relative to the scene simultaneously, we have limited the search space to linear and rotational motions only to reduce the computation time.

[12] We have considered two approaches for optimizing an antenna array. The first consists in minimizing the sidelobe levels of the PSF of the array [*Haupt*, 1995; *Kogan*, 2000; *Hebib et al.*, 2006]. The second aims to achieve a uniform coverage of the (u, v) plane [*Keto*, 1997; *Ruf*, 1993; *Kopilovich*, 2005] in order to minimize the effective redundancy. Even when the array is used in a scanning mode, both approaches still usually optimize the snapshot characteristics of the array, although *Ruf* [1990] considers its scanned characteristics. Best configurations for uniform (u, v) coverage are believed to have been found for up to 30 elements in 1-D [*Ruf*, 1993] and 2-D [*Kopilovich*, 2005]. We have chosen to maximize the uniformity of the (u, v) coverage. This leaves the possibility to apply a tapering window to reduce the sidelobe levels near the central peak if it is required.

3.1. Array Motion

[13] In this section we consider the properties of linear and rotational scans in order to determine which is more efficient for short-range imaging applications such as personnel scanning.

3.1.1. Translation

[14] When antenna signals are correlated by pairs while the array is in translation relative to the source, eg along the x-axis, as in RADSAR [*Edelsohn et al.*, 1998], the spatial frequency recorded by each baseline decreases as the array is translated away from a source. This is easily shown by consideration of a point source that lies along the x-axis (φ = 0) at a range R from a horizontal baseline with antennas 1 and 2, respectively, at ($-D$/2, 0, 0) and (D/2, 0, 0). Using equation (10) one obtains the horizontal spatial frequency u recorded by this baseline as a function of the zenith angle θ. In the far-field one can show that $\Delta r_{12} \approx D \sin\theta$ and $u(\theta) \approx D/\lambda_0 \cos\theta$. Hence the spatial frequency recorded by this baseline is maximum at zenith. In the near-field case, the exact expression of Δr_{12} must be taken into account. The spatial frequency recorded as a function of the zenith angle θ is obtained using equation (10):

$$u(\theta) = \frac{1}{\lambda_0 \cos\theta}\left(\frac{\frac{D}{2}(a+b) + R\tan\theta(a-b)}{ab}\right), \quad (17)$$

with:

$$a = \sqrt{1 + \frac{D\cos\theta(D\cos\theta - 4R\sin\theta)}{4R^2}},$$
$$b = \sqrt{1 + \frac{D\cos\theta(D\cos\theta + 4R\sin\theta)}{4R^2}}. \quad (18)$$

In this case one can show that if $R \geq D$, then $u(\theta)$ reaches maximum at zenith and decreases with θ. This means that translating the array relative to the source does not provide dense coverage at high spatial frequencies. Figure 3a shows an array of 14 antennas evenly distributed along a Reuleux triangle [*Keto*, 1997]. This array is then translated along the x-axis as shown in Figure 3b. Figures 3c and 3d present the snapshot (u, v) coverage of this array at boresight and at the scan position x = 2 m, respectively. Figure 3e shows the (u, v) coverage achieved after 10 translations between x = 0 m and x = 3 m. Note the higher density of measurements recorded at low spatial frequencies.

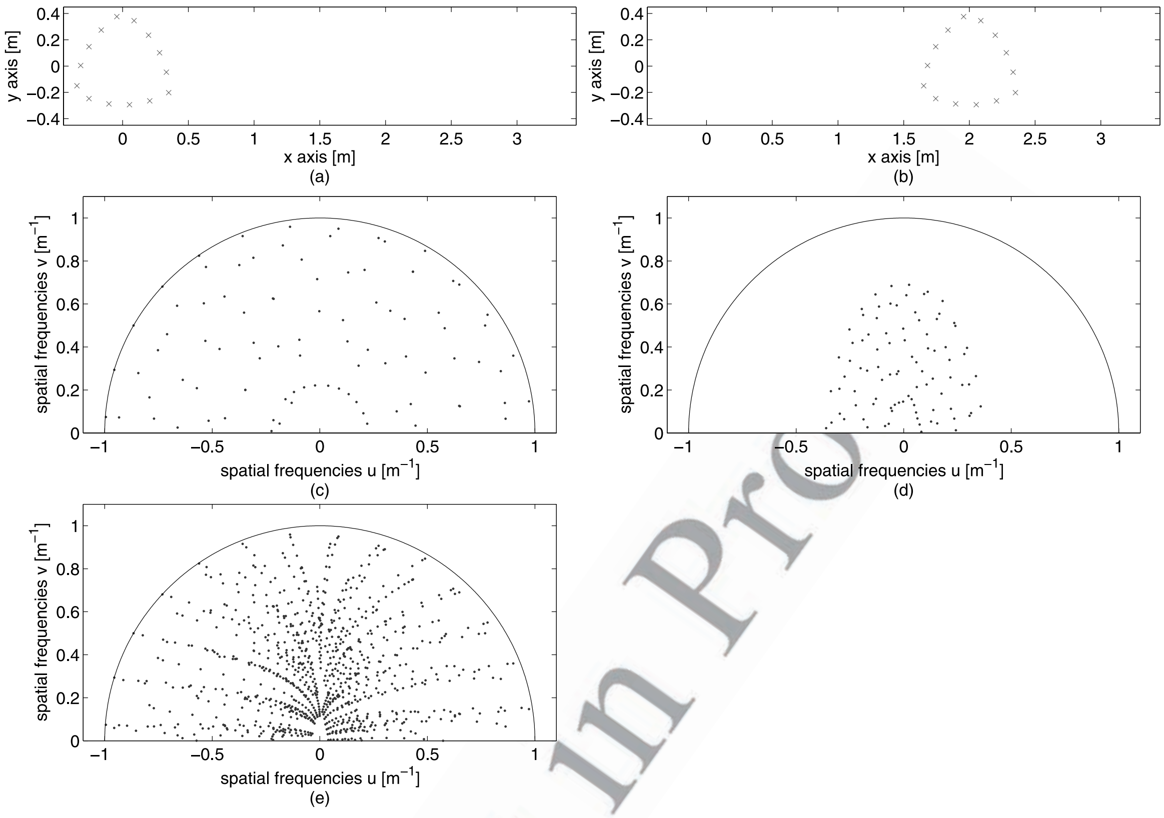

Figure 3. (a) Evenly distributed Reuleux triangle array with 14 antennas centered at the source origin $(x, y) = (0, 0)$. (b) Same array translated by 2 m along the x-axis. (c) and (d) Snapshot spatial frequency coverage of the array shown in Figures 3a and 3b, respectively. (e) Spatial frequency coverage achieved when the array is translated by increments of 0.3 m up to 3 m.

3.1.2. Rotation

[15] When the array is rotated about the Z-axis, the spatial frequencies recorded are also rotated. Figure 4 presents the (u, v) coverage of the array shown in Figure 3a after 10 rotations by 6°. Comparing the (u, v) coverage on Figure 3e and Figure 4 shows that a rotational scan clearly achieves higher relative density of measurements at high spatial frequencies compared with a linear scan and a more even coverage overall. A major issue when linear scans are employed for personnel scanning applications, is the relatively long scan path required to fill the (u, v) plane. On the other hand, this example illustrates that a rotational scan about the Z-axis efficiently yields uniform (u, v) coverage without significantly increasing the size of the system. Furthermore the logistics of rotational scanning are in practice generally simpler and more amenable to high frame-rates than is the reciprocating motion required for linear scans. As a consequence, we have chosen to maximize the uniformity of the (u, v) coverage for rotationally scanned arrays.

3.2. Array Design

[16] When optimizing the (u, v) coverage of antenna arrays, one has to cope with multiple local minima. To tackle this issue we employed a genetic algorithm (GA) [*Haupt*, 1995; *Marcano and Duràn*, 2000]. We use the

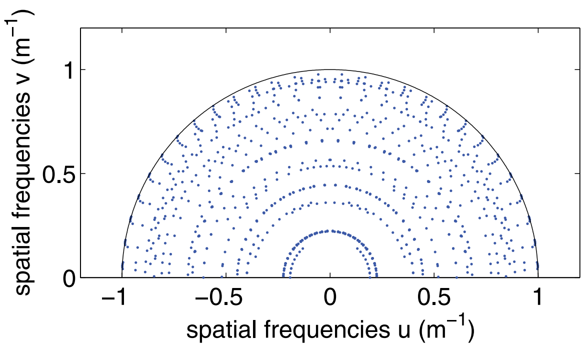

Figure 4. (u, v) coverage of the array shown in Figure 3a when rotated around the z-axis by increments of 6° up to 60°.

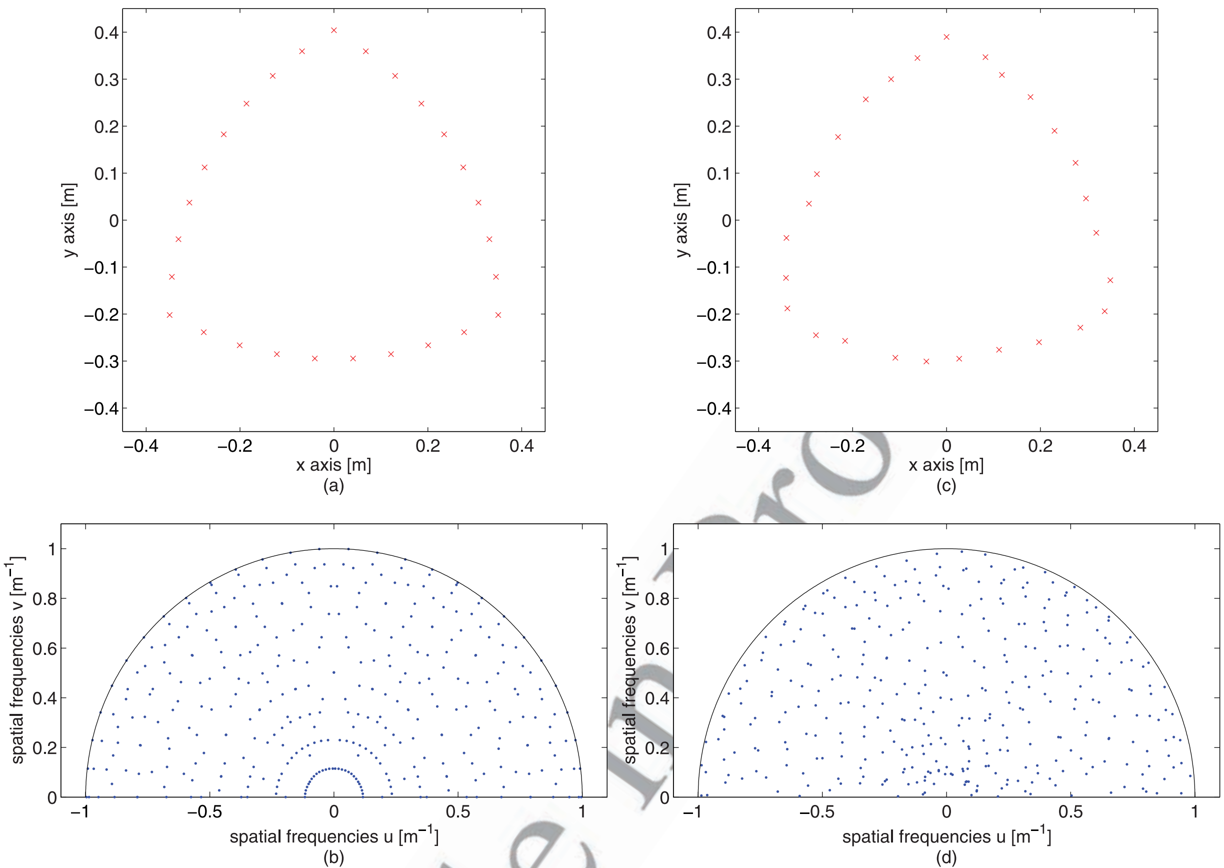

Figure 5. (a) and (b) Evenly distributed Reuleux triangle array with 27 antennas and its snapshot (u, v) coverage. (c) and (d) 27 antennas Reuleux triangle array, optimized for maximum uniform (u, v) coverage after a rotational scan of 60° in 52 steps, and its snapshot (u, v) coverage. FoV = 28°, ν_0 = 94 GHz, D = 0.7 m, R = 2 m.

differential entropy $H_{\rm diff}$ of the probability density of the (u, v) samples as a metric of the uniformity of their distribution. The differential entropy is maximized when the (u, v) samples are uniformly distributed. *Kozachenko and Leonenko* [1987] have derived an unbiased estimator of the differential entropy based on the nearest neighbor distances d_j between samples, see also *Victor* [2002] for more information. The estimator $\widehat{H}_{\rm diff}$ of the differential entropy is given by:

$$\widehat{H}_{\rm diff} = \log_2\left[\pi(M-1)\right] + \frac{\gamma}{\ln 2} + \frac{2}{M}\sum_{j=1}^{j=M}\log_2 d_j. \quad (19)$$

where γ = 0.5772156649 is the Euler-Mascheroni constant. *Cornwell* [1988] proposed a similar, more computationally expensive metric based on the sum of the logarithm of all the $M(M-1)/2$ distances between samples instead of the M nearest neighbor distances here. The use of the logarithm is rationalized there to concentrate on closely spaced samples. The maximization of the differential entropy and its estimation in equation (19) provides a rigorous justification for the use of the logarithm and the nearest neighbor distances only. Because of the $2Nn_t$ dimension of the search space, the solution obtained from the GA is likely to depend on the initial antenna positions; therefore a 'good' initial configuration is required. Since we seek isotropic sampling of the (u, v) plane, arrays in the shape of curves of constant width are natural candidates [*Keto*, 1997]. When antennas are evenly distributed along curves of constant width with a rotational degree of symmetry n (invariance to a $2\pi/n$ rotation), the (u, v) cover exhibits a degree of rotational symmetry $2n$. Therefore antenna arrays distributed along Reuleux triangles (n = 3) provide (u, v) coverage with the smallest degree of rotational symmetry among the shapes of constant width. This configuration is used as the

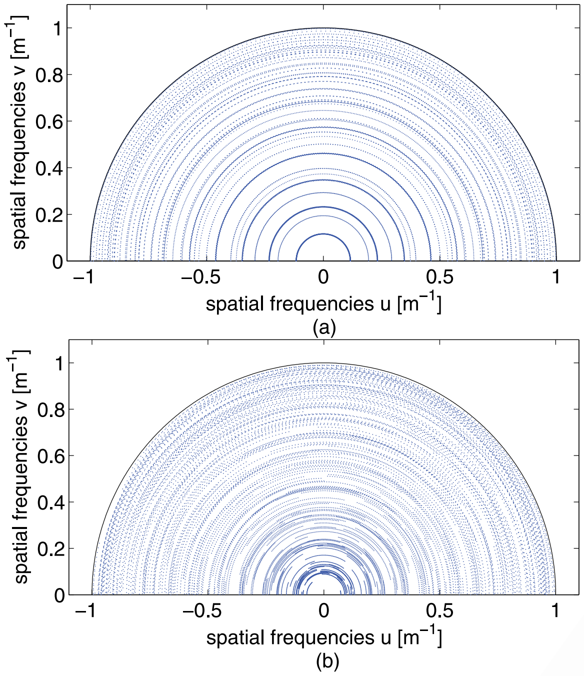

Figure 6. (a) and (b) (u, v) coverage at boresight after rotational scanning of the arrays shown in Figures 5a and 5c, respectively.

starting configuration of the GA. The motion considered is a rotation of $\pi/3$rad about the z-axis. Figures 5a and 5b present an evenly distributed Reuleux triangle array with 27 antennas and its snapshot (u, v) coverage. This array could operate at a frame-rate of 0.1 Hz with a radiometric sensitivity of 2 K. Figure 5c shows a Reuleux triangle array optimized for maximum uniform (u, v) coverage after a rotational scan of 60° in 52 steps. Figure 5d shows the snapshot (u, v) coverage of this optimized array. Figures 5 and 6 enable a comparison of the snapshot and scanned (u, v) coverage before and after optimization. The optimization clearly yields more even coverage. Figure 7 shows the PSF obtained after scanning for the nonoptimized and optimized arrays. The full width at half maximum (FWHM) of these two PSFs are both equal to 0.2°. The level of the first sidelobes are very similar; −9.4 dB and −8.9 dB for the nonoptimized and optimized arrays, respectively. This sidelobe can only be improved by tapering the (u, v) cover, and is equal to −8.9 dB in the case of a perfectly uniform coverage. However the level of higher order sidelobes is greatly reduced by the optimization as can be seen on Figure 7c. This improvement can be measured by the ratio of the energy in the main beam to the energy in the sidelobes, which is increased by a factor of 3.4 by the optimization procedure.

[17] The improved imaging performances provided by the optimized Reuleux triangle array are illustrated here with simulated images. To that end, the mm-wave brightness temperature image of a human body with an embedded rectangular metallic object is modeled

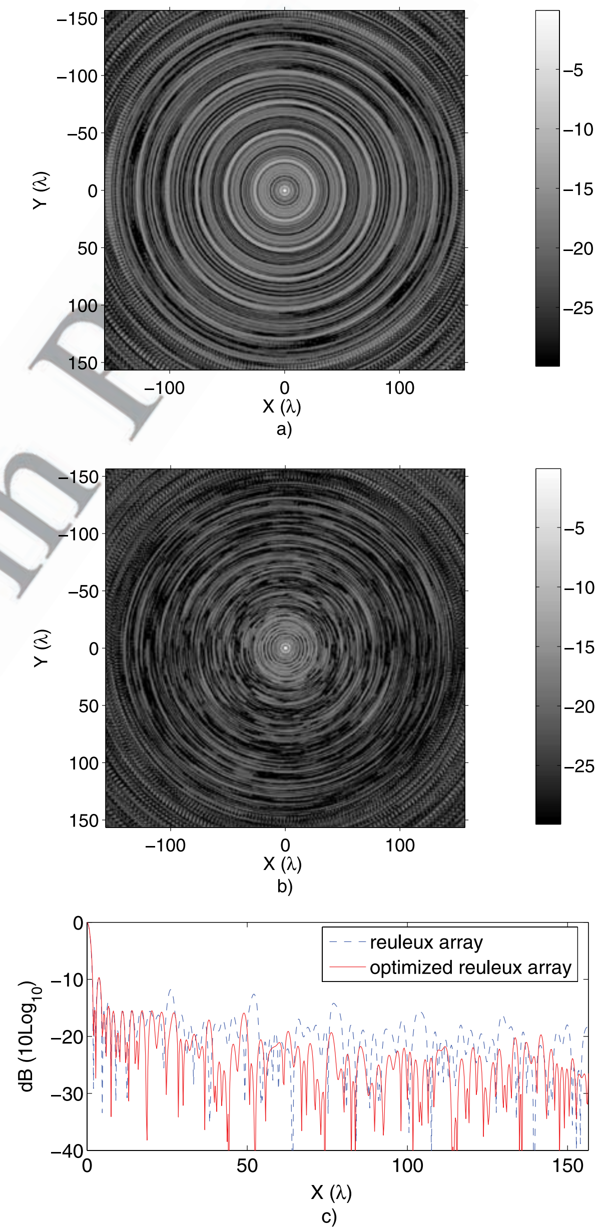

Figure 7. (a) and (b) Density plots in dB ($10Log_{10}(|PSF|)$) of the PSF at boresight of the array shown in Figures 5a and 5c, respectively, after rotational scanning. (c) One-dimensional plot of the PSF shown in Figures 7a and 7b: $PSF(x, y = 0)$.

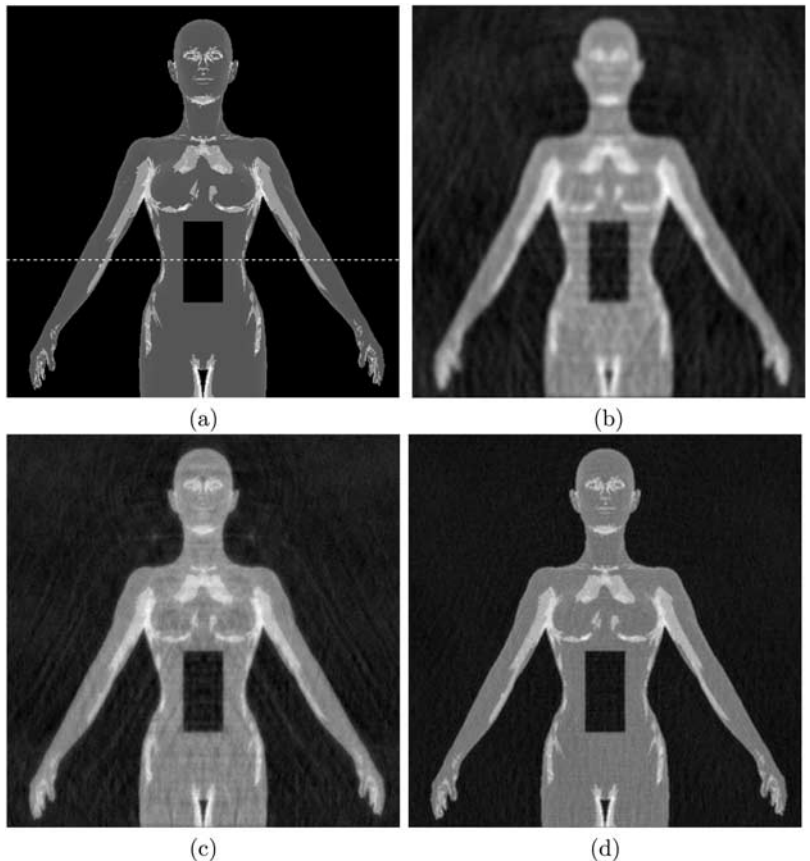

Figure 8. Imaging performances of various antenna arrays. (a) Simulated mm-wave image of a human body including a rectangular metallic object. Noise level in the recorded images is $\Delta T = 2$ K and corresponds to a 43 dB SNR. (b), (c), and (d) Images restored with the Wiener filter and recorded with the Y-shaped array, the Reuleux triangle array and the optimized Reuleux triangle array, respectively.

[*Grafulla-Gonzáles et al.*, 2006] (see Figure 8a). The body and metallic object have a uniform temperature of 290 K and the imaging system is passive. The changes observed in the measured brightness temperature are related to variations in emissivity across the scene due to the angular dependence of the Fresnel relations at a dielectric interface. We assume the angular distribution of the brightness temperature incident from the background is constant and stable over the acquisition time. The image recorded by the array is simulated by the convolution of this raw image with the PSF of the antenna array, and the addition of a white gaussian noise with a power of $4K^2$. This corresponds to a SNR of 43 dB in the recorded image. A Wiener filter is then used to restore the image. This process is performed with three arrays that each have 27 antennas and include a rotational scan of 60° in 52 steps. The first array is a power law Y-shaped array with α = 1.7 [*Chow*, 1972; *Thompson et al.*, 2001], the other two arrays are the preoptimized and postoptimized arrays shown in Figures 5a and 5b. Figures 8b, 8c and 8d show the restored images obtained with the Y-shaped array, the Reuleux triangle array and the optimized Reuleux triangle array, respectively. Figure 9 is a horizontal one-dimensional plot of the raw and restored images. Note this plot incorporates the metallic object. The image obtained with the evenly distributed Reuleux triangle array (Figure 8c) appears sharper than the image obtained with the Y-shaped array (Figure 8b) due to its higher density of measurements at high spatial frequencies. The sharpness of the image is further improved with the optimized array, where noticeably lower levels of artifacts are present. The root-mean-square (RMS) error between the restored images and the raw image are 5.6%, 4.7% and 3.3% for the images shown in Figures 8b, 8c and 8d, respectively. These values are averages over

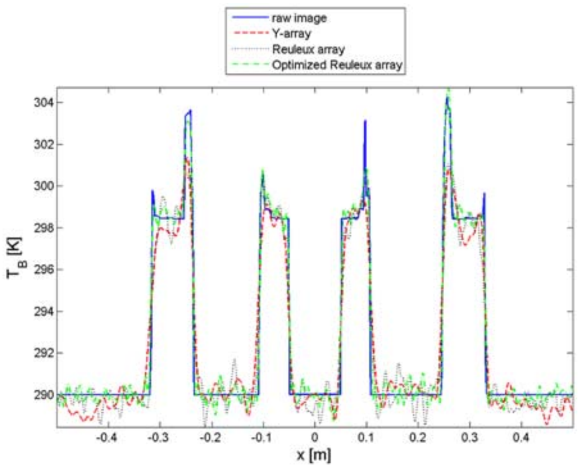

Figure 9. Imaging performances of various antenna arrays. One-dimensional plot of the restored images including the metallic object.

10 observations. This endorses the better imaging performances provided by the Reuleux triangle arrays compared with the Y-shaped array and illustrates the improvements provided by the optimization of the array.

3.3. Reduction of Bandwidth Decorrelation

[18] We have stated in section 2.1 that the amplitude modulation of the visibility function due to the fringe-wash function can be greatly reduced by introducing delay lines in the antenna channels. Since the delay lines must be introduced before the correlator, an additional correlator is included for each artificial delay line introduced. We seek now to estimate the number of delay-lines required. To that end we estimate the period $X_{IP_{nm}}$ of the interference pattern and the position $X_{FW_{nm}}$ of the first null of the fringe-wash function. To simplify the analysis we consider a horizontal baseline with coordinates $(-D_{nm}/2, 0, 0)$ and $(D_{nm}/2, 0, 0)$. Using equations (4) and (6) we obtain $X_{IP_{nm}}$ and $X_{FW_{nm}}$:

$$X_{IP_{nm}} = \frac{\lambda_0}{2}\sqrt{1 + \frac{4R^2}{D_{nm}^2 - \lambda_0^2}}. \tag{20}$$

$$X_{FW_{nm}} = \frac{c}{2\Delta\nu}\sqrt{1 - \frac{4R^2}{\left(\frac{c}{\Delta\nu}\right)^2 - D_{nm}^2}}. \tag{21}$$

The interference patterns must be translated by ΔX_{nm} so that they sum in-phase. The translation $\Delta X_{nm} = \mathrm{Round}\left(\frac{X_{FW_{nm}}}{X_{IP_{nm}}}\right) X_{IP_{nm}}$ provides a reasonable amplitude modulation after adding all the translated interference patterns (no amplitude below 96%). Thus the number of delay lines for the baseline (n, m) is $\mathrm{Round}\left(\frac{2x_{\max}}{\Delta X_{nm}}\right)$. Finally, the number, $\mathcal{N}$, of delay lines and correlators to be introduced to compensate for the fringe-wash function can be estimated as follow:

$$\mathcal{N} = \sum_{n=1}^{N} \sum_{m=n+1}^{N} round\left(\frac{2x_{max}}{\Delta X_{nm}}\right). \tag{22}$$

For the array shown in Figure 5c, we estimate $\mathcal{N} \approx 4000$.

[19] The subband implementation described in section 2.1 requires a correlator per baseline and per subband. For the system considered in this paper the 15 GHz bandwidth would have to be divided into approximately 30 subbands in order to record 90% of the signal at the edges of the 28° FoV. This leads to a total number of correlators of 10500, more than 2.5 times the number of correlators required with the delay lag implementation. However this technique has the significant advantage to require narrow band correlators instead of both wide-band correlators and delay lines. It therefore seems preferable to implement. In addition, since both implementations require a number of correlator that increases with the number of baselines, the sequential acquisition of the visibility data in n_t iterations enables a reduction in the number of correlators by the same factor compared with a snapshot array.

4. Impact of Instabilities on Image Quality

4.1. Instrument Instabilities

[20] Time-sequential acquisition of the visibility function will normally reduce the number of short antenna baselines and hence the effects of mutual coupling between receivers should be reduced, simplifying calibration of this effect. Conversely the increased time necessary to record the required visibilities increases sensitivity to drift in electronic gain and offset of the receivers and correlators compared to snapshot acquisition. In many short-range imaging applications for which the proposed technique is of interest, real-time calibration may be implemented by recording the visibilities for calibration images which incorporate point-source beacons. If the recording of calibration images is multiplexed with the recording of scene images, we calculate that a calibration time of ~2 seconds is required, in addition to a total acquisition time of 10 seconds, in order to attain a calibration accuracy of 2 K [*Torres et al.*, 1997]. It is of interest however to consider the impact of drift in the absence of such on-line calibration. We address this by supposing a linear drift with time in the gain and offset of the recorded correlations and compare the image quality of a snapshot imager with that of a sequential imager. For each baseline (m, n), we assume

errors introduced in the original calibration to be negligible. The measured visibility $\widetilde{\mathcal{V}}_{mn}$ may be written as:

$$\widetilde{\mathcal{V}}_{mn} = \mathcal{V}_{mn} G_{mn}(t) + O_{mn}(t) \tag{23}$$

with $\mathcal{V}_{mn}$ the true visibility, $G_{mn}(t)$ and $O_{mn}(t)$ the complex gain and offset of the instrument, respectively. The drift rates in the real and imaginary parts of the gain and offset of the correlator output are simulated by random variables with zero mean Gaussian distribution and standard deviation σ. We have calculated the RMS error ε in the synthesized image with gain and offset errors for 10 observations (to account for the random nature of the instrument drift). For the rotational scanning system shown in Figure 5c, $n_t = 52$, simulations showed (1) the RMS errors in the visibility data and in the restored images are both linear functions of the RMS drift rate and (2) the RMS error in the restored images for the scanning system is increased by a factor $\sim$58 compared with that of a snapshot imager. This corresponds to a significantly more challenging calibration problem.

4.2. Background Illumination

[21] In the simulations illustrated in Figure 8 images comparison, the scene illumination is from ambient surroundings and is considered to be constant with time and uniform in angular distribution [*Grafulla-González et al.*, 2006]. For applications such as personnel scanning it will be possible for the background and illumination to be kept relatively constant during the acquisition times considered here, however, the longer acquisition times of the proposed technique will increase sensitivity to temporal changes in average illumination compared to a snapshot technique.

5. Conclusions

[22] We have demonstrated that in synthetic aperture near-field mm-wave imaging, time-sequential recording of the visibility function offers a route to reduced antenna count and hence the potential for reduced complexity. If the visibility function is recorded with n_t time-sequential samples during which the antenna is either rotated or translated, point-spread-function quality can be maintained for a factor $\sqrt{(n_t)}$ reduction in the number of antennas and a factor n_t reduction in the number of correlators. Rotation is shown to more efficiently sample the spatial frequencies of the scene, particularly after optimization. The simplification is obtained at the cost of a deterioration in radiometric sensitivity, which can be recovered only by a factor n_t increase in the total integration time. In principle, for certain applications where long integration times are feasible, acceptable sensitivity of 2 K could be obtained for systems in which the number of antennas is an order of magnitude lower than for snapshot systems. The longer integration times introduce greater demands on system stability however which may require improved or real-time calibration.

[23] **Acknowledgments.** This work has been funded by the UK Technology Strategy Board and QinetiQ.

References

Appleby, R. (2004), Whole body 35 GHz security scanner, *Proc. SPIE*, *5410*, 244–251.

Chow, Y. L. (1972), On designing a supersynthesis antenna array, *IEEE Trans. Antennas Propag.*, *20*, 30–35.

Cornwell, T. J. (1988), A novel principle for optimization of the instantaneous Fourier plane coverage of correlation arrays, *IEEE Trans. Antennas Propag.*, *36*(8), 1165–1167.

Edelsohn, C., J. Gurley, H. McCord, R. Donnelly, P. Virga, W. Butler, and A. Jain (1998), RADSAR (RADiometric SAR) experimental results, in *International Geoscience and Remote Sensing Symposium*, pp. 372–374, IEEE Press, Piscataway, N. J.

Grafulla-González, B., K. Lebart, and A. R. Harvey (2006), Physical optics modelling of millimetre-wave personnel scanners, *Pattern Recognition Lett.*, *27*(15), 1852–1862.

Harvey, A. R., and R. Appleby (2003), Passive mm-wave imaging from UAVs using aperture synthesis, *Aeronaut. J.*, *107*(1068), 87–97.

Haupt, R. L. (1995), An introduction to genetic algorithms for electromagnetics, *IEEE Antennas Propag. Mag.*, *37*(2), 7–15.

Hebib, S., N. Raveu, and H. Aubert (2006), Cantor spiral array for the design of thinned arrays, *IEEE Antennas Wireless Propag. Lett.*, *5*, 104–106.

Keto, E. (1997), The shapes of cross-correlation interferometers, *Astrophys. J.*, *475*, 843–852.

Kogan, L. (2000), Optimizing a large array configuration to minimize the sidelobes, *IEEE Trans. Antenna Propag.*, *48*(7), 1075–1078.

Kopilovich, L. E. (2005), Non-redundant hexagonal array configurations for optical interferometric systems compactly covering central domains in the spatial-frequency plane, *J. Modern Opt.*, *52*(10), 1415–1420.

Kozachenko, L. F., and N. N. Leonenko (1987), On statistical estimation of entropy of random vector, *Problems Infor. Transmiss.*, *23*(2), 95–101, (translated from Problemy Peredachi Informatsii (in Russian), 23 (2), 9–16).

Marcano, D., and F. Duràn (2000), Synthesis of antenna arrays using Genetic Algorithms, *IEEE Antennas Propag. Mag.*, *42*(3), 12–20.

Peichl, M., H. Suess, M. Suess, and S. Kern (1998), Microwave imaging of the brightness temperature distribution of extended areas in the near and far field using two-dimensional aperture synthesis with high spatial resolution, *Radio Sci.*, *33*(3), 781–801.

Ruf, C. S. (1990), Antenna performance for a synthetic aperture microwave radiometer in geosynchronous earth orbit, *Int. Geosci. Remote Sens. Symp.*, *2*, 1589–1592.

Ruf, C. S. (1993), Numerical annealing of low-redundancy linear arrays, *IEEE Trans. Antennas Propag.*, *41*(1), 85–90.

Ruf, C. S., C. T. Swift, A. B. Tanner, and D. M. L. Vine (1988), Interferometric synthetic aperture microwave radiometry for the remote sensing of the earth, *IEEE Trans. Geosci. Remote Sens.*, *26*(5), 597–611.

Sheen, D. M., D. L. McMakin, and T. E. Hall (2001), Three-dimensional millimeter-wave imaging for concealed weapon detection, *IEEE Trans. Microwave Theory Tech.*, *49*(9).

Thompson, A. R., J. M. Moran, and G. W. Swenson (2001), *Interferometry and Synthesis in Radio Astronomy*, John Wiley, Hoboken, N. J.

Torres, F., A. Camps, J. Bará, and I. Corbella (1997), Impact of receiver errors on the radiometric resolution of large 2D aperture synthesis radiometers: Study applied to MIRAS, *Radio Sci.*, *32*(2), 629–641.

Victor, J. D. (2002), Binless strategies for estimation of information from neural data, *Phys. Rev.*, *66*(051903), 1–15.

____

B. Grafulla-González, Research Department, New Technology Multimedia, Ericsson AB, Sölvegatan 53, SE-221 83 Lund, Sweden.

A. R. Harvey and B. M. Lucotte, School of Engineering and Physical Sciences, Heriot-Watt University, Riccarton Campus, Edinburgh EH14 4AS, UK. (a.r.harvey@hw.ac.uk; bl13@hw.ac.uk)